



# Investigation on Fracture Properties of Single-Flawed Tunnel Model Under Medium-to-Low-Speed Impacts

Lei Zhou<sup>1</sup>    Zheming Zhu<sup>2\*</sup>    Ruifeng Liu<sup>2</sup>     Yong Fan<sup>2</sup>    Yuqing Dong<sup>2</sup>  
Peng Ying<sup>2</sup>

<sup>(1)</sup>State Key Laboratory of Hydraulics and Mountain River Engineering, College of Architecture and Environment, Sichuan University, Chengdu 610065, China)

<sup>(2)</sup>Key Laboratory of Deep Underground Science and Engineering (Ministry of Education), College of Architecture and Environment, Sichuan University, Chengdu 610065, China)

Received 7 January 2019; revision received 16 July 2019; Accepted 24 July 2019;  
published online 8 August 2019

© The Chinese Society of Theoretical and Applied Mechanics 2019

**ABSTRACT** Dynamic fractures occur frequently in geophysical processes and engineering applications. It is thus essential to study crack and failure behaviors, such as crack time-to-initiation, crack growth rate and arrest period under dynamic loading. In this study, impact experiments were implemented by utilizing the single-flawed tunnel specimens under drop-hammer impacts. Four brittle materials, i.e., green sandstone, red sandstone, black sandstone and polymethyl methacrylate, were selected to make single-flawed tunnel specimens. Strain gauges and crack extension gauges were employed to measure the crack extension parameters. The properties of crack growth rate, crack time-to-initiation and arrest period of these four brittle materials were discussed and analyzed. The corresponding numerical simulation was performed by using the commercial software AUTODYN. The numerical results of crack growth rate and crack time-to-initiation agreed with the impact test results. The commercial software ABAQUS was applied to compute the dynamic stress intensity factors. The results show that both the dynamic initiation fracture toughness and the crack growth rate increase with the elastic moduli of these four types of brittle materials under the same loading conditions, whereas the crack time-to-initiation decreases with the increase in elastic moduli of the brittle materials under the same loading conditions.

**KEY WORDS** Single-flawed tunnel, Impact loading, Crack growth rate, Crack time-to-initiation, Initiation fracture toughness

## 1. Introduction

Dynamic fractures are frequently encountered in earthquake-induced faulting, impact-and-collision-induced fracturing, blast-induced fragmenting and so on [1], which significantly affect the stability of underground structures. It is thus imperative to perform the corresponding research to better understand the dynamic fracture mechanism, and to guide the designers in enhancing underground structures' stability and preventing geological disasters. The crack or joint emanating from tunnel edges has an adverse effect on tunnel stability, and the corresponding investigation on the fracture behaviors of crack under different loading rates is of great concern [2]. In the present research, experimental and

\* Corresponding author. E-mail: zhemingzhu@hotmail.com

simulation studies of the influence of crack on tunnel stability are implemented using the sandstone and PMMA tunnel specimens containing single radial cracks located at the tunnel roofs.

A modified split-Hopkinson pressure bar (SHPB) test equipment has been extensively adopted in the research of dynamic responses of various brittle materials under impact loads [3–6]. However, there still remain a number of unsolved problems which could affect the test results, such as the friction between the bars and the specimen [7, 8], the choice of slenderness ratio of the specimen, the necessity of dynamic stress equilibrium [9, 10] and the validity of the standard equation in the data reduction [11–13]. The maximum diameter of the incident and transmitted bars of conventional SHPBs are about 100 mm, and the specimen configuration needs to be less than the maximum diameter of the incident and transmitted bars according to the SHPB theory. The specimen of small configuration could produce some effects of the tensile reflected wave on crack and failure behaviors [14, 15]. Thus, a large-dimension single-flawed tunnel specimen of 300 mm × 350 mm × 30 mm was proposed in this study. The drop-hammer testing equipment set up in accordance with the principle of SHPB and suitable for large-specimen tests was applied.

Numerical simulations can not only be used to validate the test results, but also be applied to describe the crack and failure behaviors under various dynamic loading conditions and reveal the crack behavior at micro-levels, which cannot be performed in dynamic experiments [16–18]. Thus, numerical simulation plays an indispensable role in studying the failures of brittle materials. Ma and An [19] utilized the commercial software LS-DYNA to simulate the blast-caused dynamic fractures of rock; Zhu et al. [20–22] applied the extended RFPA-Dynamics software to simulate the damage evolution and stress distribution in rock samples by utilizing the traditional SHPB tests. Redish et al. [23] utilized a drop-weight testing machine and the FLAC3D model to investigate the influence of impact speed on the failure behavior of cylindrical granite specimens. In the present study, the reputable commercial software AUTODYN, based on the finite difference approach, was applied because of its superiority in solving the problems of geometric nonlinearity and material nonlinearity under dynamic loads [24–31]. The Lagrange processor was applied, and the governing formulas of mass conservation, momentum conservation and energy conservation were employed.

The present paper aims to investigate the fracture properties of four brittle materials under medium-to-low-speed impacts, and meanwhile, tries to find a suitable method for measuring the crack dynamic parameters of brittle materials. A large-dimension single-flawed tunnel specimen was used, and impact tests were implemented by utilizing the single-flawed tunnel samples. The crack extension parameters were determined by utilizing the crack extension gauges (CEGs). The dynamic stress intensity factors (DSIFs) were computed through utilizing the finite element software ABAQUS [14]. Subsequently, crack growth rate, crack time-to-initiation and arrest period were investigated by using the finite difference software AUTODYN.

## 2. Impact Equipment and Specimens

The drop-hammer testing equipment designed on the basis of conventional SHPB test equipment was applied in the present study, as depicted in Fig. 1. LY12CZ aluminum alloy was selected as the material of the incident bar, which is much lighter than steel; and steel was selected as the material of the transmitted bar. The mechanical parameters are given in Table 1. The incident bar has a length of 3 m, the transmitted bar has a length of 1 m, and the cross sections of the bars are both 0.3 m × 0.03 m (width × thickness). During the impact tests, an HG59 copper plate was mounted at the top of the incident bar to minimize the dispersion effect [32].

The signals of the incident strain, reflected strain and transmitted strain, i.e.,  $\varepsilon_i(t)$ ,  $\varepsilon_r(t)$ , and  $\varepsilon_t(t)$ , were recorded by the strain gauges mounted reliably on the incident and transmitted bars. A four-channel digital oscilloscope manufactured by RIGOL was used to record the strain signals. According to the strains, the calculations of stress  $\sigma_1(t)$  on the top of the specimen and  $\sigma_2(t)$  at the bottom are given by Eqs. (1) and (2) [33, 34], respectively:

$$\sigma_1(t) = E_i \frac{A_i}{A_S} [\varepsilon_i(t) + \varepsilon_r(t)] \quad (1)$$

$$\sigma_2(t) = E_t \frac{A_t}{A_S} \varepsilon_t(t) \quad (2)$$

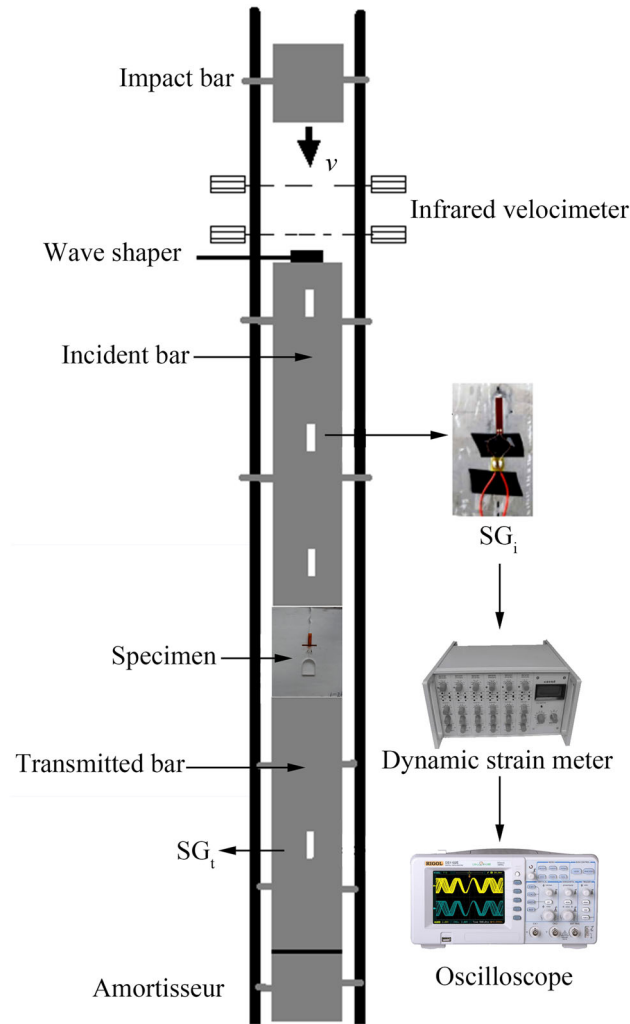


Fig. 1. Drop-hammer impacting test system

Table 1. Mechanical parameters of brittle materials

Material	$\rho$ (kg/m <sup>3</sup> )	$E$ (GPa)	$\mu$	$c_1$ (m/s)	$c_2$ (m/s)	$c_R$ (m/s)
LY12CZ	2850	71.7	0.3	5006	–	–
Steel	7850	210	0.28	5200	–	–
Green sandstone	2265	13.58	0.21	2563	1607	1479
Red sandstone	2229	24.50	0.19	2897	1758	1604
Black sandstone	2580	33.67	0.17	3781	2339	2126
PMMA	1135	6.1	0.25	2160	1450	1292

where the indices  $i$ ,  $r$ ,  $t$  and  $s$  represent the incident, the reflected, the transmitted and the specimen, respectively,  $E$  represents the elastic modulus, and  $A$  represents the cross-sectional area.

The dimension of the single-flawed tunnel specimen has a length of 350 mm, a width of 300 mm and a thickness of 30 mm, with a centralized tunnel and a radical crack, as shown in Fig. 2. The pre-crack length is fixed at 50 mm, and the thickness is less than 1 mm. The pre-crack was fabricated through a steel blade, and the crack tip must be sharpened according to the requirements of the International Society for Rock Mechanics (ISRM). The height and width of the tunnel are 50 mm and 60 mm, respectively, and the arc radius is 25 mm. Twenty specimens (i.e., 5 green sandstone specimens, 5 red

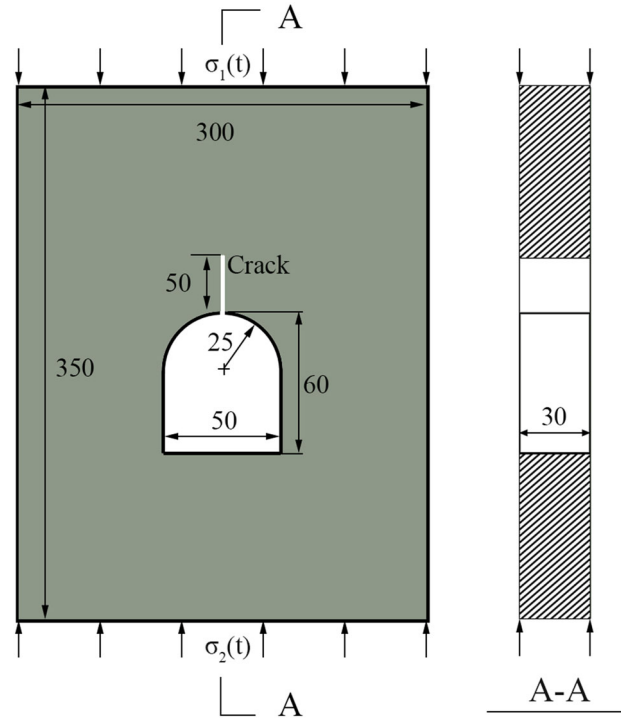


Fig. 2. Schematics of a typical specimen (unit: mm)

sandstone specimens, 5 black sandstone specimens and 5 PMMA specimens) were prepared and tested in this study.

The sandstone and polymethyl methacrylate (PMMA) specimens are compact and uniform, as shown in Fig. 3. The experimental results for PMMA indicated that the fracture behavior under dynamic loading was similar to those revealed in the isotropic and homogeneous sandstone [35, 36]. Besides, featured with good transparency and homogenization, the crack extension patterns of PMMA can be observed readily. Thus, except for three types of sandstone, PMMA ( $C_5H_8O_2$ ) was also adopted in the present study.

The dilatational wave speed  $c_1$  and shear wave speed  $c_2$  of brittle materials were evaluated by the Sonic Viewer-SX, as shown in Fig. 4. For each brittle material, there were six specimens, all of which were made with the size of 50 mm  $\times$  100 mm (diameter  $\times$  length). The test results are presented in Table 1.

The typical measuring results of strain-gauge signals for the green sandstone specimen #1 are plotted in Fig. 5a. The stress-time histories are shown in Fig. 5b, and these curves can be used as the input loads in the succeeding simulation.

### 3. Experimental Studies

Impact tests were implemented by utilizing the single-flawed tunnel specimens under the drop-hammer impacts. The crack time-to-initiation, the spreading time at different locations along the crack extension trajectory and the crack growth rate are required for the computation of the critical DSIFs by means of the experimental–numerical approach [37]. In order to measure these parameters, CEGs (type BKX5-10CY-21-W) were glued along the crack extension trajectories, as shown in Fig. 6. The CEGs are made of a group of filaments, the number of which is designed by taking into account the crack extension trajectories pre-evaluated. The available scope of the CEGs in this study was 44 mm, and the interval between two adjacent filaments was 2.2 mm. The CEG measuring technique is illustrated in Fig. 6. The power was provided by a constant voltage source (16 V).  $R_{C2}$  was connected in series with the CEG in the electrical circuit, and  $R_{C1}$  was connected in parallel, in order to protect the CEG from overload damage.

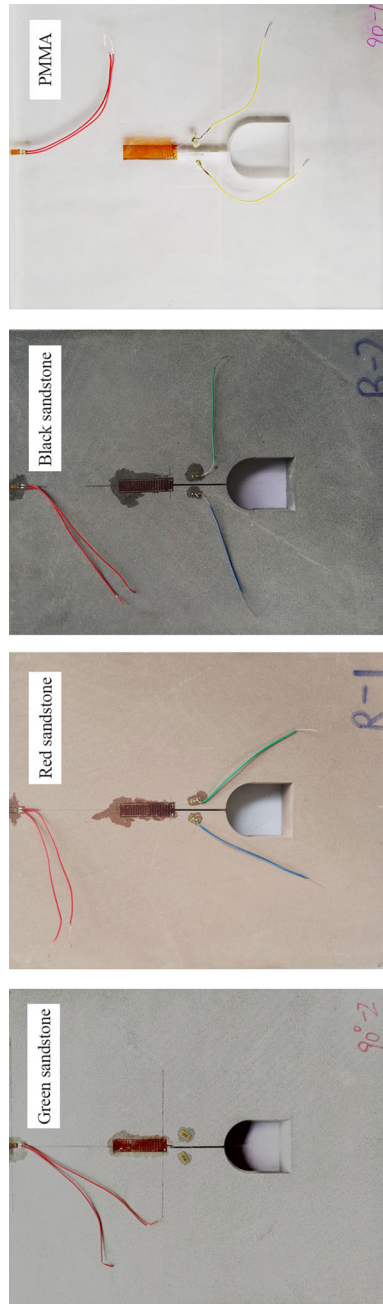


Fig. 3. Single-flawed tunnel model specimens of brittle materials

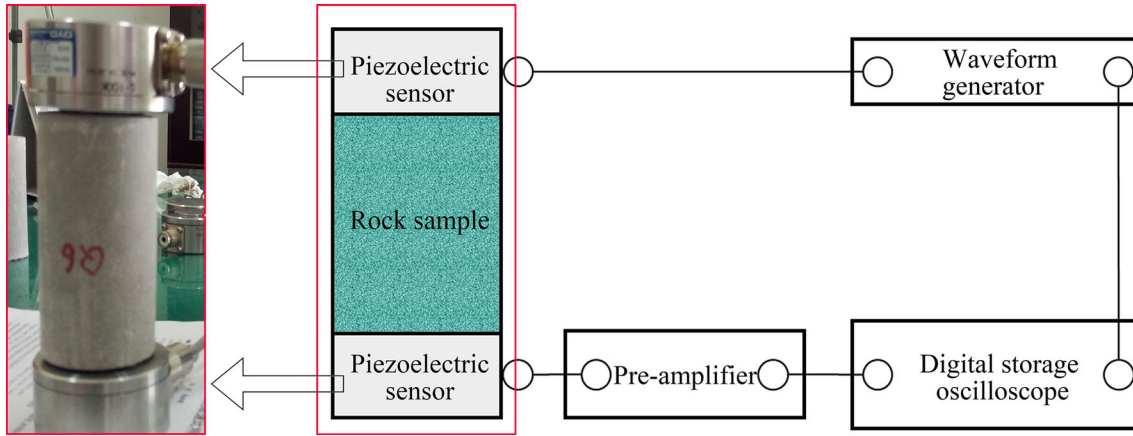


Fig. 4. The dilatational wave speed  $c_1$  and shear wave speed  $c_2$  by ultrasonic methods

### 3.1. Crack Time-to-Initiation Determined by Strain Gauge

As a stress wave reaches the crack tip, the initiation of crack usually does not occur immediately, but takes a short period of time. The difference between the initiation time of the crack and the time when the stress wave reaches the crack tip is defined as the crack time-to-initiation.

The measuring results of the PMMA specimen #2 by using the CEG are presented in Fig. 7. We can find that at the moment  $t_i = 317.5 \mu\text{s}$ , the 1st filament of the CEG was fractured, leading to a sudden increase in the voltage signal. This phenomenon indicates that the pre-crack starts to propagate.

To validate the CEG test results, a large strain gauge was glued on the reverse side near the crack tip reliably. At the time  $317.5 \mu\text{s}$ , the strain gauge was also fractured very fast and the voltage signal reading increased abruptly. One can find that the CEG test results are reliable in the impact tests. According to the measuring results, the crack time-to-initiation for the PMMA specimen #2 is  $317.5 \mu\text{s}$ .

### 3.2. Measurements of Crack Time-to-Initiation and Crack Growth Rate by CEG

The 1st filament of CEG coincides with a crack tip, and the fracture of the 1st filament can be considered as the instant of crack initiation. When the crack continues to extend, the CEG filaments will become fractured sequentially, and the corresponding voltage signal of the CEG collected is a step-by-step history. The time corresponding to the maximum value of the derivative of voltage signal with respect to time can be deemed as the filament fracture time. According to the fracture time and the interval distance between two adjacent filaments, the instantaneous crack growth rate can be calculated. The results for green sandstone specimen #1, red sandstone specimen #2, black sandstone specimen #1 and PMMA specimen #1 under the impact velocities of 8.376 m/s, 8.385 m/s, 8.302 m/s and 8.373 m/s, respectively, are depicted in Fig. 8.

For all the sandstone specimens, no arrest phenomena can be observed clearly during crack extension, whereas for the PMMA specimen in Fig. 8d, in two periods, the crack took a relatively long time to pass the two adjacent filaments, and the crack may be arrested in these two periods.

All the test results of the dynamic parameters are listed in Table 2. The average values of fracture parameters for each brittle material were calculated, as shown in Table 3. The average impact velocities of these brittle materials are similar. The average crack growth rates of green sandstone, red sandstone and black sandstone as well as the PMMA are 577.922 m/s, 703.942 m/s, 828.611 m/s and 210.335 m/s, respectively. For PMMA, the average crack growth rate is the lowest, and the speed ratios of the green, red and black sandstone to the PMMA are 2.75, 3.35 and 3.94, respectively. One can conclude that the crack growth rate increases with material elastic modulus under the impacts of the same speed.

The average crack time-to-initiation of PMMA is  $317.1 \mu\text{s}$ , which is the longest of the four brittle materials; whereas for the black sandstone, it is  $220.5 \mu\text{s}$ , which is the shortest. The difference between the average crack time-to-initiation of PMMA and that of the black sandstone is  $96.6 \mu\text{s}$ . One can

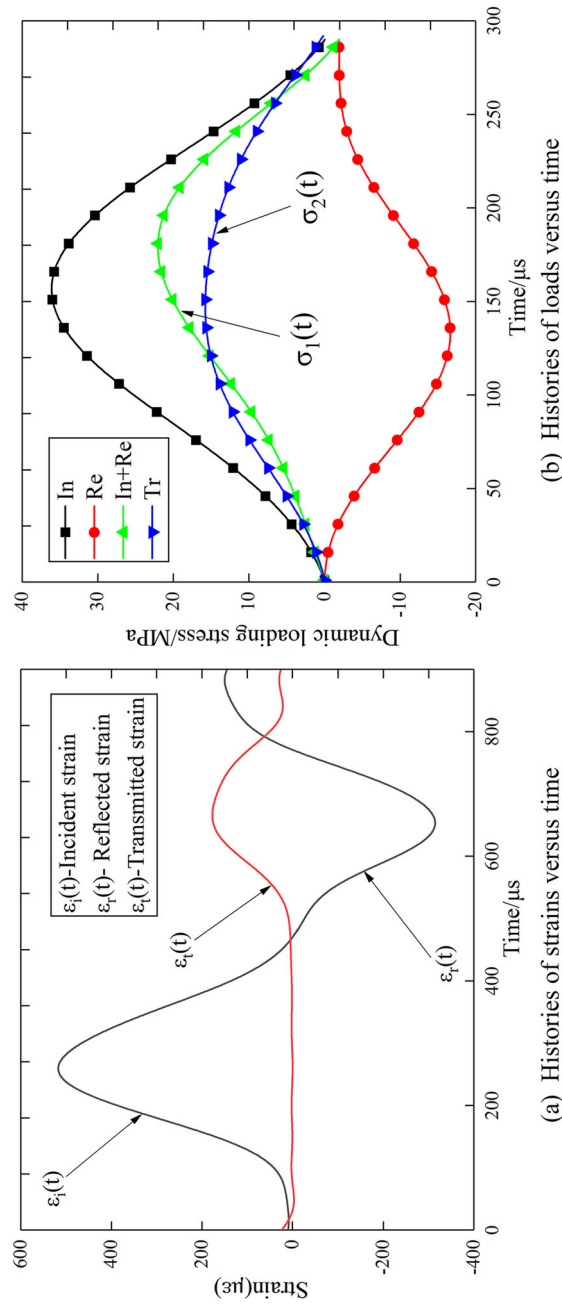


Fig. 5. The measured strain and loading histories of a typical green sandstone specimen

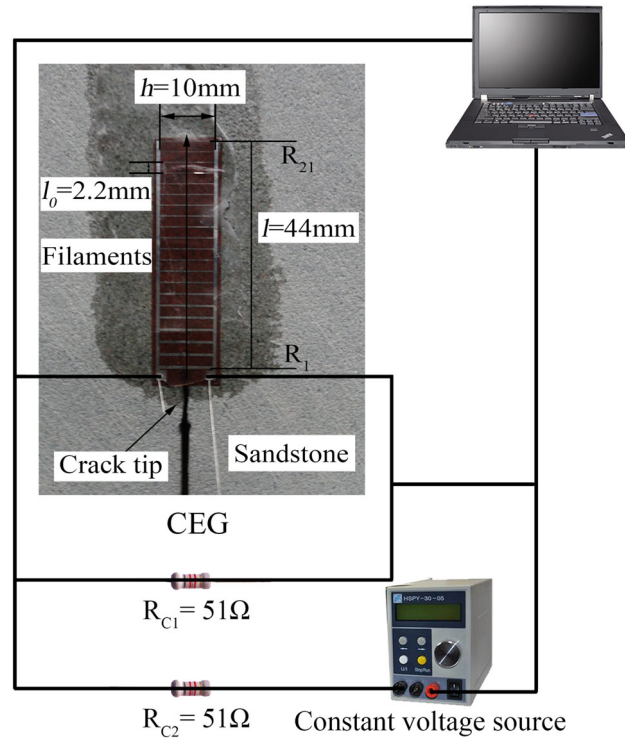


Fig. 6. CEG test technique

conclude that the crack time-to-initiation decreases with the increase in material elastic modulus under the impacts of the same speed.

## 4. Numerical Models and Evaluation of Critical SIFs

### 4.1. Computation of the Dynamic Stress Intensity Factors (DSIFs)

In order to compute the dynamic stress intensity factors (DSIFs), several two-dimensional single-flawed numerical tunnel models for the specimens tested in this study under impact loading were built on the basis of the specimen geometry illustrated in Fig. 2 and the mechanical parameters presented in Table 1. The quarter-node triangle elements CPS6 were adopted to discretize the zones near the crack tips, whereas the eight-node quadrilateral elements CPS8 were adopted for other zones, as depicted in Fig. 9. The whole tunnel model contains 1486 elements and 16,233 nodes. The history of  $\sigma_1(t)$  from Fig. 5 was loaded to the incident end of the specimen, and the history of  $\sigma_2(t)$  from Fig. 5 was loaded to the transmitted end of the specimen. The gravity of the specimens was also considered in the numerical models.

To compute precisely the DSIFs, the crack in tunnel can be deemed as an ideal sharp flaw, and the elements near the crack tip were densified. Based on the theory of traditional fracture mechanics, we used the time histories of the displacement of nodes A and B obtained by the commercial software ABAQUS to compute the mode I SIF  $K_I(t)$  as follows:

$$K_I(t) = \frac{E}{24(1-\mu^2)} \sqrt{\frac{2\pi}{r_{OA}}} [8v_A(t) - v_B(t)] \quad (3)$$

where  $E$  and  $\mu$  represent elastic modulus and Poisson's ratio, respectively;  $r$  represents radius; and  $v_A(t)$  and  $v_B(t)$  represent the time histories of the vertical displacement of node A and node B, respectively.



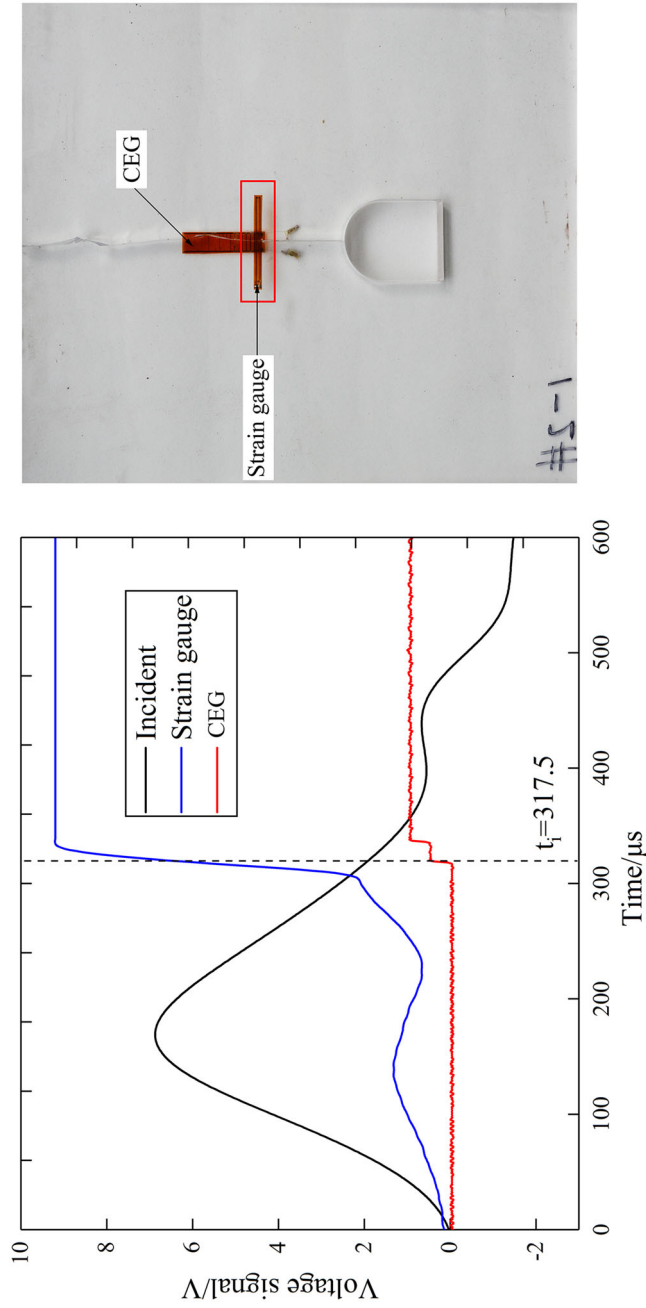


Fig. 7. The crack initiation of PMMA specimen #2 measured by a CEG and a strain gauge

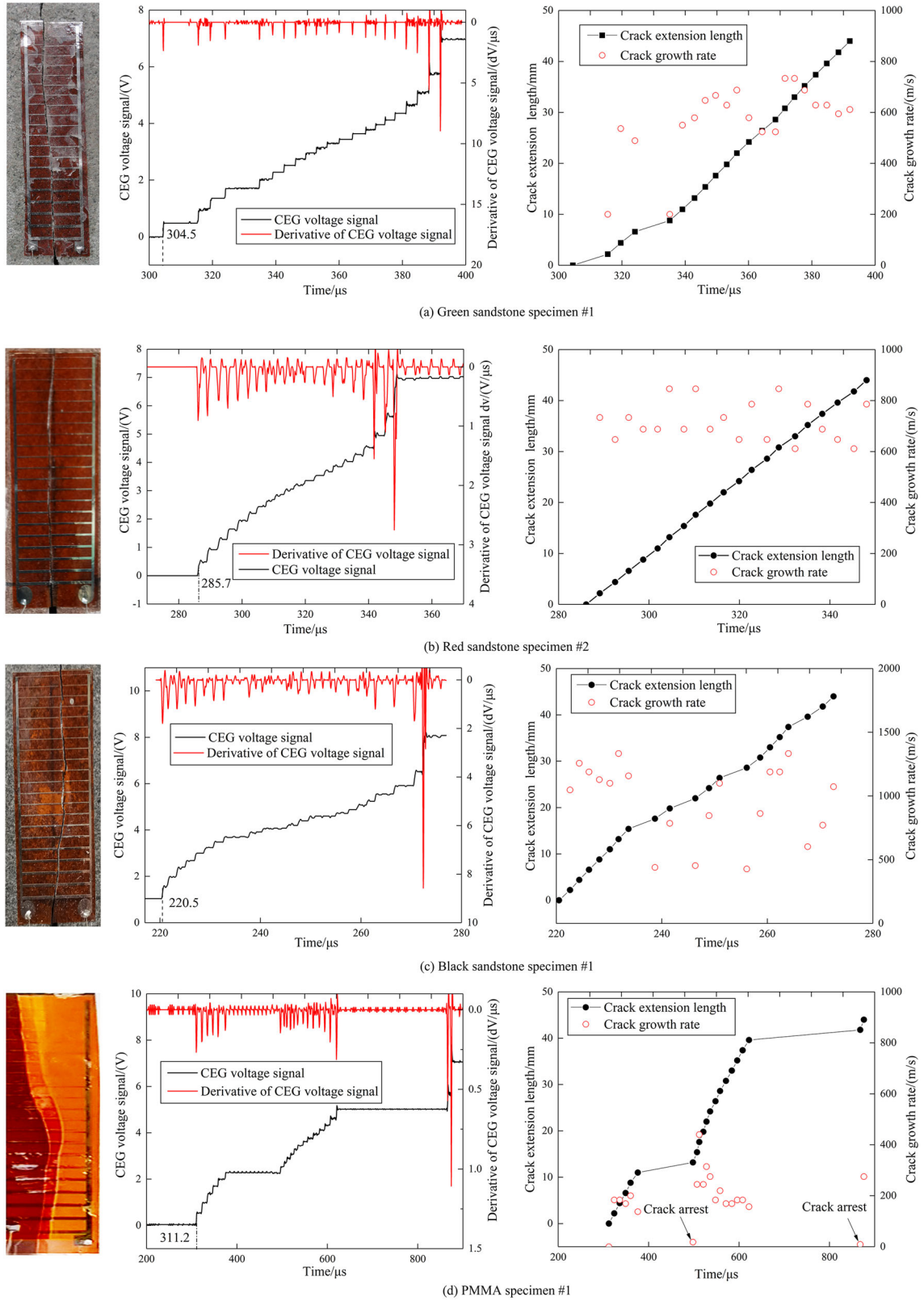


Fig. 8. The CEG test results

Table 2. Impact test results

Material	Impact velocity (m/s)	Maximum crack growth rate (m/s)	Minimum crack growth rate (m/s)	Average crack growth rate (m/s)	Crack time-to-initiation ( $\mu\text{s}$ )	Crack arrest period ( $\mu\text{s}$ )	Initiation fracture toughness ( $\text{MPa m}^{0.5}$ )
Green sandstone	8.376	733.333	200.000	502.857	304.5	–	2.76
	8.303	997.957	271.605	423.484	295.5	–	3.02
	8.292	1157.895	611.111	695.103	297.8	–	2.26
	8.332	709.677	226.804	577.428	301.5	–	2.81
	8.357	916.667	536.585	690.738	287.7	–	2.65
Red sandstone	8.380	846.154	611.111	709.677	266.7	–	3.37
	8.385	907.478	541.325	751.265	285.7	–	2.86
	8.311	880.888	244.444	746.930	261.7	–	2.58
	8.191	753.809	229.167	523.583	272.5	–	2.55
	8.507	811.223	311.54	788.256	272.9	–	3.15
Black sandstone	8.302	1333.333	427.184	831.758	220.5	–	3.56
	8.311	1222.545	547.424	899.456	254.3	–	2.89
	8.324	1412.012	612.547	911.245	232.7	–	2.76
	8.292	1111.476	512.447	655.276	252.4	–	3.77
	8.607	1275.456	412.246	845.321	224.3	–	3.64
PMMA	8.373	314.286	137.500	202.041	311.2	246.02/122.00	2.02
	8.284	297.297	84.615	207.329	317.5	310.20/749.5	2.54
	8.347	270.936	147.059	211.855	295.2	265.72/417.03	1.85
	8.471	257.009	125.142	196.702	325.7	279.44/760.12	1.73
	8.289	314.286	137.511	233.750	335.8	274.32/282.53	3.11

Table 3. Average fracture parameters of four brittle materials

Material	Average impact velocity (m/s)	Average crack growth rate (m/s)	Average crack time-to-initiation ( $\mu\text{s}$ )	Average initiation fracture toughness ( $\text{MPa m}^{0.5}$ )
Green sandstone	8.332	577.922	304.5	2.70
Red sandstone	8.354	703.942	266.7	2.91
Black sandstone	8.367	828.611	220.5	3.32
PMMA	8.352	210.335	317.1	2.25

#### 4.2. Initiation Fracture Toughness (IFT)

For the case of green sandstone specimen #1, according to the loading history as shown in Fig. 5 and the specimen geometry, the numerical model was built by utilizing the software ABAQUS. The dynamic stress intensity factors (DSIFs) of the crack were computed, and the curve of DSIFs is illustrated in Fig. 10a. At the preliminary stage, the DSIFs are negative. This is to be expected because when the stress wave just reached the crack tip, the crack tip was under compression. The experimental result of the crack time-to-initiation was  $304.5 \mu\text{s}$ , and then the value of  $2.76 \text{ MPa } \sqrt{\text{m}}$  in the vertical axis that corresponds to  $304.5 \mu\text{s}$  in the horizontal axis is the critical DSIF, which can be deemed as the initiation fracture toughness (IFT) of the green sandstone.

Similarly, for the specimens of red sandstone, black sandstone and PMMA, the calculation results of the histories of DSIFs are depicted in Fig. 10b–d, respectively. According to the calculation results of crack time-to-initiation, the corresponding critical DSIFs can be determined and the results are  $K_I^D(t) = 3.37 \text{ MPa } \sqrt{\text{m}}$ ,  $3.56 \text{ MPa } \sqrt{\text{m}}$ , and  $2.02 \text{ MPa } \sqrt{\text{m}}$  in the present study, respectively.

Table 3 also presents the test results of the average dynamic IFT of sandstone and PMMA under the same impact loads, and they are  $3.32 \text{ MPa } \sqrt{\text{m}}$ ,  $2.91 \text{ MPa } \sqrt{\text{m}}$ ,  $2.70 \text{ MPa } \sqrt{\text{m}}$  and  $2.25 \text{ MPa } \sqrt{\text{m}}$ , for the black sandstone, red sandstone, green sandstone and PMMA, respectively. It is found that the dynamic IFT of the black sandstone is the highest; and that of the PMMA is the lowest, only 67%

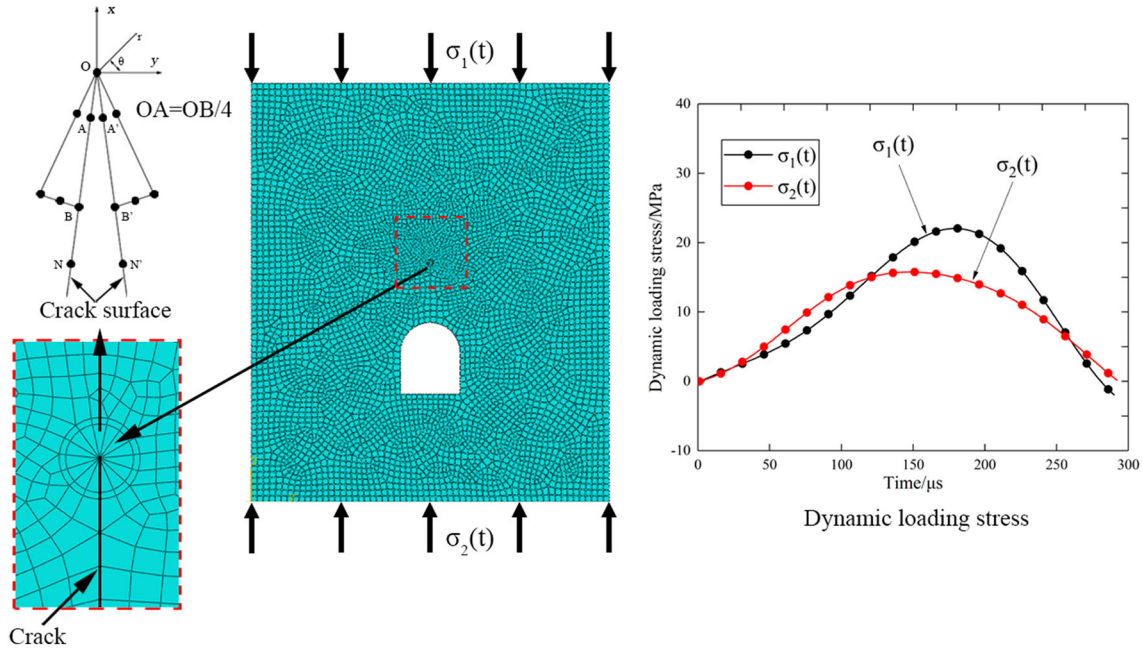


Fig. 9. Mesh elements and dynamic loads used in the ABAQUS software

of the former. One can conclude that the dynamic IFT increases with material elastic modulus (or P-wave speed).

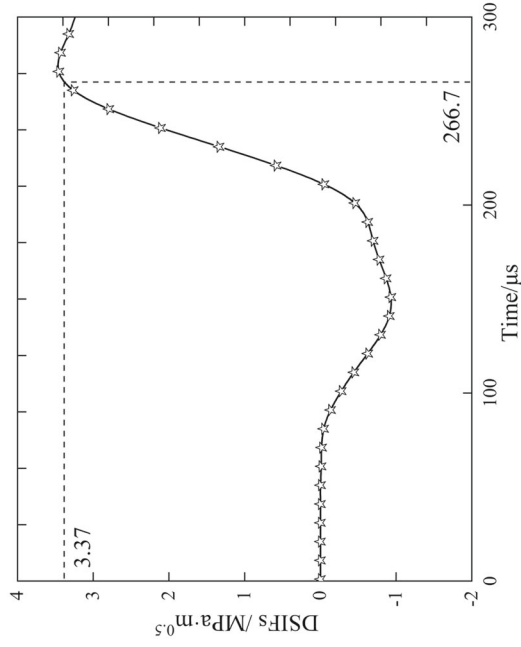
In order to clearly understand the reason for the difference of dynamic initiation fracture toughness between different brittle materials under impact loads, microscopic studies were performed to give an insight of the failure surfaces of brittle materials near crack tips by utilizing the scanning electron microscope (SEM), as shown in Fig. 11. When the failure surfaces near crack tips are amplified to 200 or 300 times, the mineralogical compositions of sandstone and PMMA can be observed. One can find that the porosity of black sandstone is the largest, whereas PMMA almost has no pores, and the porosities of red sandstone and green sandstone stay in between. This explains why the crack growth rate of black sandstone fluctuates obviously and is the largest. The failure surface of the black sandstone is the roughest, those of the red sandstone and green sandstone are flatter, and that of the PMMA is the flattest, which indicates that the black sandstone was mainly fractured due to transgranular destructions, whereas the red sandstone and green sandstone were mainly fractured due to intergranular destructions. This explains why the dynamic initiation fracture toughness of black sandstone is the greatest.

## 5. Numerical Studies

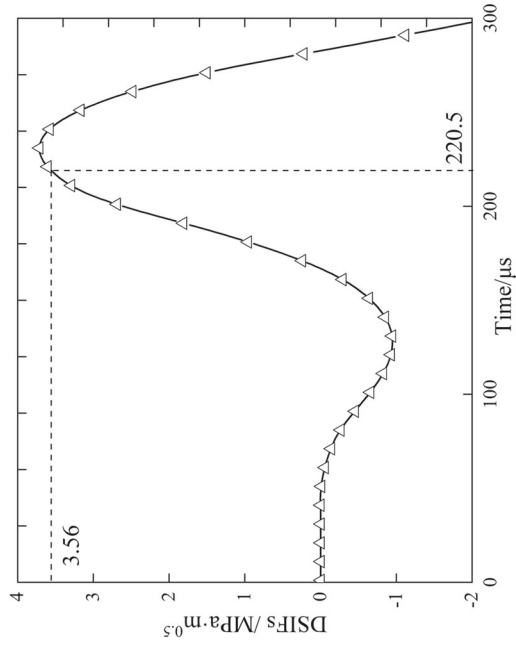
In the present study, crack initiation and extension were simulated utilizing the 2D AUTODYN software. The commercial software AUTODYN has been dramatically developed in the numerical analysis of crack and failure behaviors in various brittle materials under dynamic loads in recent years [38–40] and the experience has shown that it is able to display the simulation of crack extension trajectories.

### 5.1. Numerical Models

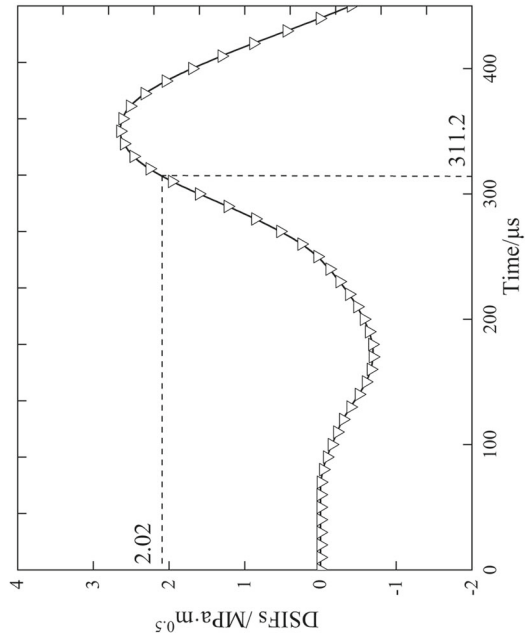
To simulate the actual impact process, finite difference models of the whole drop-hammer impact equipment under impact loads were built by utilizing the AUTODYN software in this paper. The numerical models were designed according to the dimensions, as well as the boundary and loading conditions. The two-dimensional quadrilateral elements were employed to mesh the whole impact equipment, and the number of elements is 106,060. Figure 12 shows the scaled close-up view of a typical mesh for parts of the incident and transmitted bars and the specimen. The bottom of the



(a) Green sandstone specimen #1.



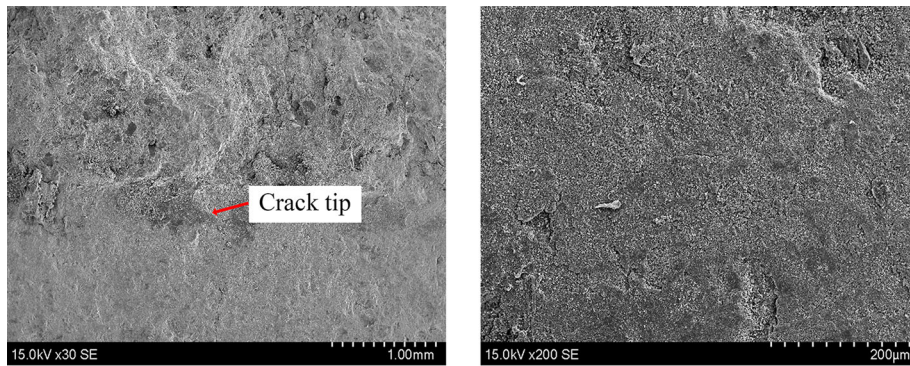
(b) Red sandstone specimen #1.



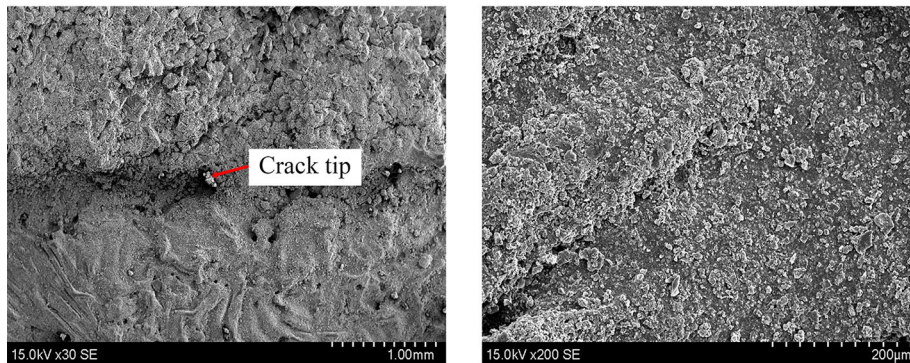
(c) Black sandstone specimen #1.

(d) PMMA specimen #1.

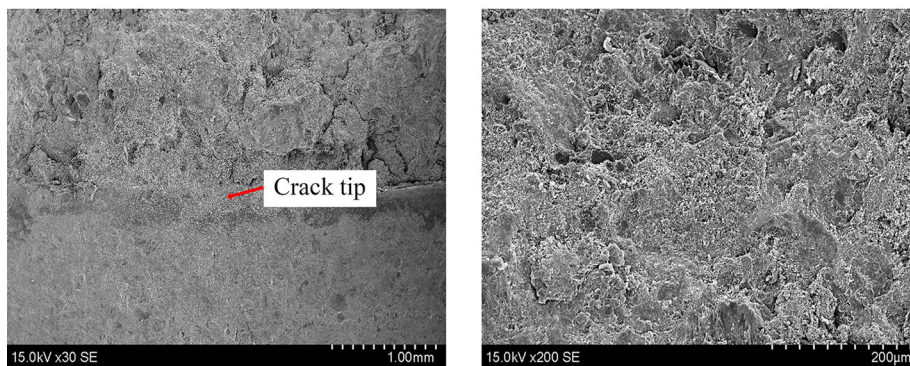
Fig. 10. The histories of DSIFs of initial cracking at the crack tip



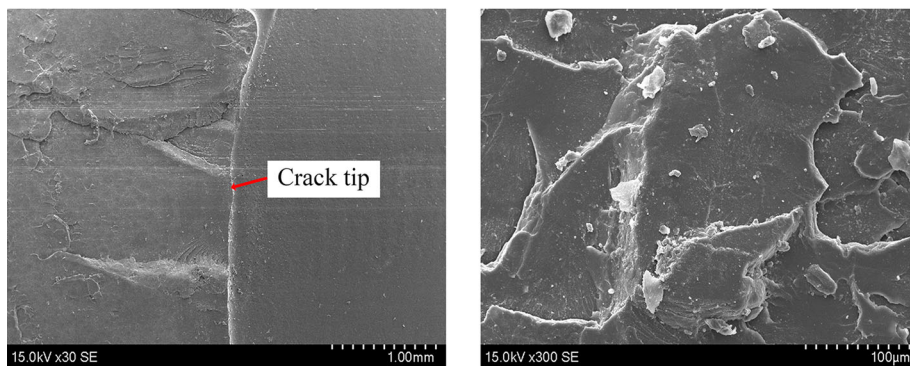
(a) Green sandstone specimen



(b) Red sandstone specimen



(c) Black sandstone specimen



(d) PMMA specimen

Fig. 11. The microstructures near the crack tips scanned by the scanning electron microscope

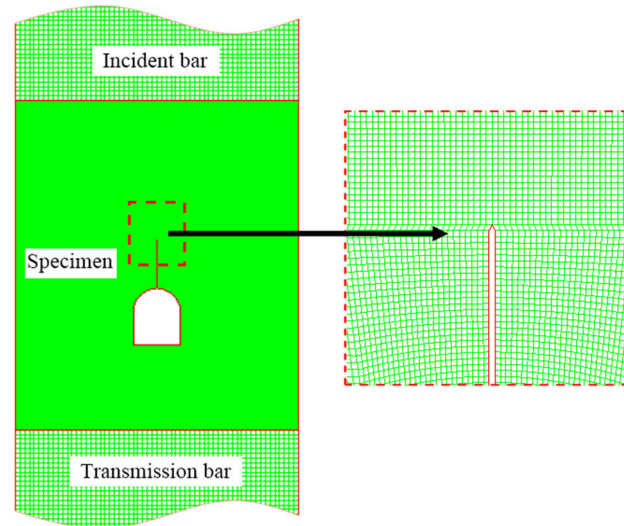


Fig. 12. Numerical model of the single-flawed tunnel

concrete amortisseur was established as the no-reflection boundary, which can minimize the influence of the reflected tensile stress wave on crack trajectories. The crack width is established according to the experimental models, and the mechanical parameters of the four types of brittle materials applied in this simulation are listed in Table 1.

In the impact tests, the pressure or deformation is relatively small; thus, the density or volumetric deformation of the brittle material is linearly related to the pressure. Thus, the linear equation of state (EOS) is adopted.

$$P = \kappa\mu = \kappa \left( \frac{\rho}{\rho_0} - 1 \right) \quad (4)$$

where  $P$  represents pressure,  $\kappa$  represents bulk modulus,  $\rho$  represents density, and  $\rho_0$  represents original density.

Failure criteria play a key role in dynamic numerical modeling, which describe material status under dynamic loading. Except for the specimen, there were no failures for other parts of the impact system. Thus, no failure criteria were employed to them. For the sandstone and PMMA specimens, the major principal stress failure criterion is adopted to describe the progressive failure. As the maximum tensile or the maximum shear stress exceeds the dynamic tensile or shear strength of a brittle material, the element fails, i.e.,

$$\sigma_1 \geq [\sigma] \quad \text{or} \quad \tau_{12} \geq [\tau_r] \quad (5)$$

where  $\sigma_1$  represents the maximum tensile principal stress,  $[\sigma]$  represents tensile strength,  $\tau_{12}$  represents the maximum shear stress, and  $\tau_r$  represents shear strength. In the numerical simulation, as an element fails, it cannot stand any tensile or shear load, but is still able to stand compressive load.

## 5.2. Numerical Analysis Results

The crack extension trajectories for the green sandstone specimen and the PMMA specimen versus time are presented in Figs. 13 and 14. In general, the numerical results are consistent with our experimental results, and the comparison indicates that this specimen configuration can satisfy the experimental requirements. In the numerical simulation, the crack trajectory is smooth, whereas in the experiments, the crack trajectory has two or three inflexions. This could be induced due to the sandstone inhomogeneity. When a crack runs into a big particle, it will bypass this particle, which may produce some inflexions along the crack extension trajectory.

The average crack growth rate of the simulation results for the green sandstone specimen was 569.43 m/s in the zone between 0 and 44 mm, in which the CEG was attached; and for PMMA

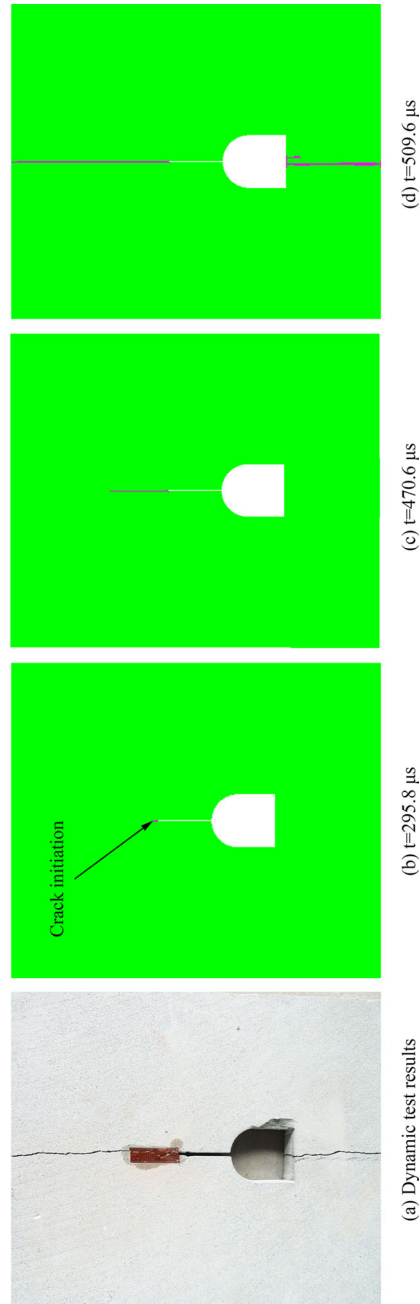


Fig. 13. The failure modes of green sandstone specimen #1



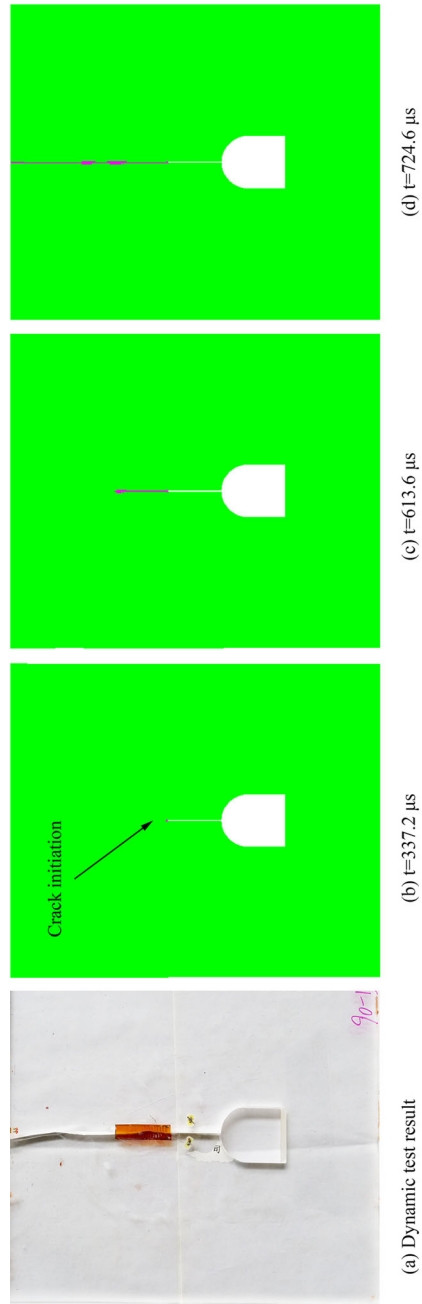


Fig. 14. The failure modes of PMMA specimen #1

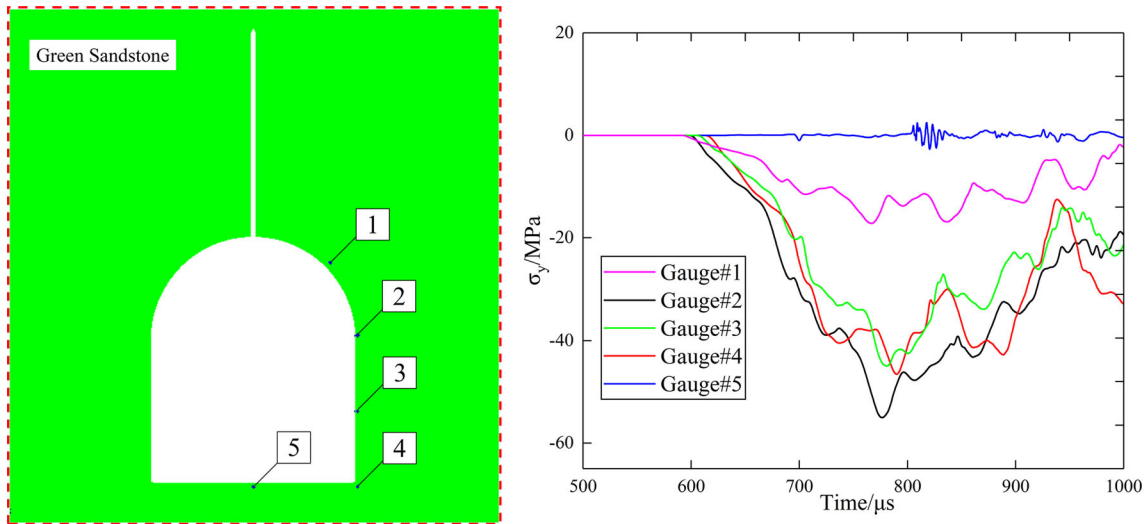


Fig. 15. The histories of normal stress  $\sigma_y$  for gauge points 1, 2, 3, 4, and 5

specimen, it was 217.789 m/s. The test results presented in Table 3 show that the average crack growth rate is 577.92 m/s for the green sandstone and 210.335 m/s for the PMMA, representing differences of 1.45% and 3.54% from the simulation results, respectively.

The crack time-to-initiation in the simulation results is 295.8  $\mu\text{s}$  for the green sandstone and 337.2  $\mu\text{s}$  for the PMMA. The experimental results presented in Table 3 show that the average crack time-to-initiation is 304.5  $\mu\text{s}$  for the green sandstone and 317.1  $\mu\text{s}$  for the PMMA. Comparing the experimental results with the numerical simulation results, one can find that the difference is 2.86% for the green sandstone and 6.34% for the PMMA.

For the green sandstone specimen, except for the extension of the preexisting crack, a new flaw formed at the bottom of the tunnel. The failure modes are significantly different from that under quasi-static loads [41–43]. However, for the case of PMMA specimen, no such cracks formed at the bottom of the tunnel.

To further investigate the fracture mechanism of the single-flawed tunnel specimen under dynamic loading, several gauge points can be set along the tunnel edge. The normal stresses  $\sigma_y$  in gauges 1, 2, 3, 4 and 5 are depicted in Fig. 15. In gauges 2 and 4 located at the tunnel spandrel and the tunnel foot, respectively, the normal stresses  $\sigma_y$  are greater than those of other gauges. In gauge 5,  $\sigma_y$  is very small, but the tensile stress is large, which caused a new vertical crack at the tunnel bottom.

## 6. Comparison and Discussion

In the conventional SHPB testing, it is usually assumed that the stresses at both ends of the specimen are balanced, and the stresses or strains are uniformly distributed along the vertical direction of the whole specimen. Nevertheless, in our tests, the crack initiated when the stress wave just reflected back from the bottom of the specimen (at the time 295.8  $\mu\text{s}$ ), as shown in Fig. 16. Apparently at this time, the forces or stresses at both ends of the specimen cannot be balance because usually the stress wave needs 3–5 times of transmission and reflection to reach balance [44]. In addition, the experimental–numerical approach was adopted to evaluate the critical SIFs, in which the stress equilibrium condition does not need to be satisfied.

## 7. Conclusion

To clearly understand the dynamic fracture properties of single-flawed tunnel, a large specimen with a single radial flaw located at the tunnel roof was employed. Four types of brittle material were selected to prepare the specimens. Impact experiments were implemented by using the single-flawed tunnel specimens. Crack time-to-initiation, spreading time and crack growth rate were determined by crack extension gauges (CEGs). Meanwhile, several simulation models were established by utilizing the

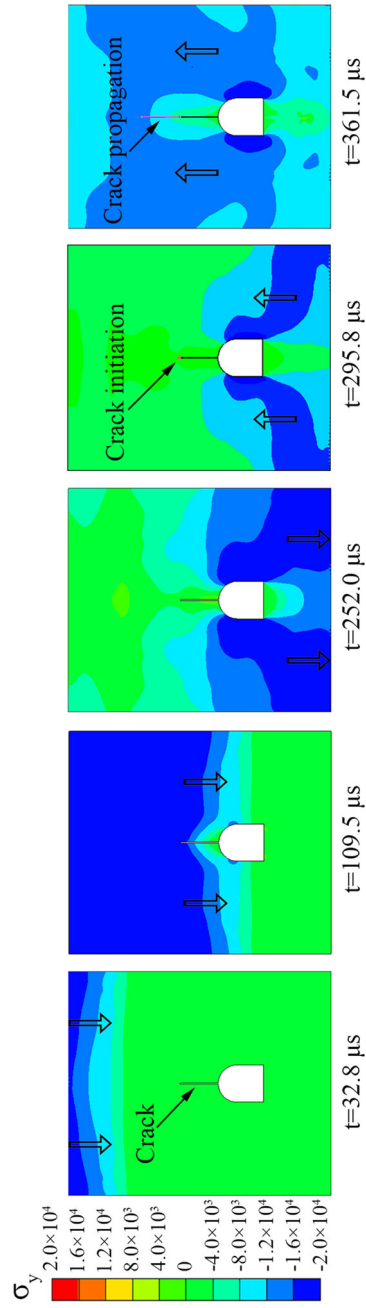


Fig. 16. The material status of green sandstone specimen influenced by the stress wave through the specimen

commercial software AUTODYN, and the numerical results of crack extension trajectory, crack time-to-initiation and crack growth rate agreed with the test results. The finite element software ABAQUS was used to compute DSIFs, and the dynamic IFT was evaluated by utilizing the experimental–numerical approach.

- (1) For the case of a crack in tunnel model under impact loads, the crack growth rate varies with the length of crack propagation. The crack growth rate of PMMA is generally smaller than those of sandstone under almost identical loading conditions, and the average crack growth rate of PMMA is about one-third of that of sandstone. Crack growth rate increases with material elastic modulus.
- (2) The crack time-to-initiation of PMMA is higher than that of sandstone under the same impact load. Crack time-to-initiation decreases with the increase in material elastic modulus. As the surrounding rock mass medium of tunnel is black sandstone, it is crucial to consider the influence of internal flaws in surrounding rock mass on tunnel stability.
- (3) The dynamic IFT of PMMA is lower than that of sandstone under the same impact load. The IFT of brittle material increases with material elastic modulus.

**Acknowledgements.** This work was financially supported by the National Natural Science Foundation of China (11672194), Sichuan Administration of Work Safety (aj20170515161307) and the Project of Science and Technology of Sichuan Province (2018JZ0036).

## References

- [1] Chen S, Wu J, Zhang Z. Blasting vibration safety criteria for shotcrete in underground engineering. *J Test Eval.* 2016;44:574–81.
- [2] Zhou H, Zhang C, Li Z, Hu D, Hou J. Analysis of mechanical behavior of soft rocks and stability control in deep tunnels. *J Rock Mech Geotech.* 2014;6(3):219–26.
- [3] Wang L, Hu S, Yang L, Sun Z, Zhu J, Lai H, Ding Y. Development of experimental methods for impact testing by combining Hopkinson pressure bar with other techniques. *Acta Mech Solida Sin.* 2014;27(4):331–44.
- [4] Xie Q, Zhu Z, Kang G. A dynamic micromechanical constitutive model for frozen soil under impact loading. *Acta Mech Solida Sin.* 2016;29(1):13–21.
- [5] Li D, Cheng T, Zhou T, Li X. Experimental study of the dynamic strength and fracturing characteristics of marble specimens with a single hole under impact loading. *Chin J Rock Mech Eng.* 2015;34(2):249–60.
- [6] Li D, Han Z, Sun X, Zhou T, Li X. Dynamic mechanical properties and fracturing behavior of marble specimens containing single and double flaws in SHPB tests. *Rock Mech Rock Eng.* 2019;52(6):1623–43.
- [7] Wang QZ, Yang JR, Zhang CG, Zhou Y, Li L, Zhu ZM, Wu LZ. Sequential determination of dynamic initiation and propagation toughness of rock using an experimental–numerical–analytical method. *Eng Fract Mech.* 2015;141:78–94.
- [8] Qiu J, Li D, Li X. Dynamic failure of a phyllite with a low degree of metamorphism under impact Brazilian test. *Int J Rock Mech Min Sci.* 2017;94:10–7.
- [9] Zhang QB, Zhao J. Determination of mechanical properties and full-field strain measurements of rock material under dynamic loads. *Int J Rock Mech Min Sci.* 2013;60:423–39.
- [10] Zhang QB, Zhao J. Effect of loading rate on fracture toughness and failure micromechanisms in marble. *Eng Fract Mech.* 2013;102:288–309.
- [11] Xia K, Yao W. Dynamic rock tests using split Hopkinson (Kolsky) bar system—a review. *J Rock Mech Geotech.* 2015;7(1):27–59.
- [12] Li XB, Lok TS, Zhao J, Zhao PJ. Oscillation elimination in the Hopkinson bar apparatus and resultant complete dynamic stress–strain curves for rocks. *Int J Rock Mech Min Sci.* 2000;37(7):1055–60.
- [13] Qiu J, Li D, Li X, Zhou Z. Dynamic fracturing behavior of layered rock with different inclination angles in SHPB tests. *Shock Vib.* 2017;2017:1–12.
- [14] Wang X, Zhu Z, Wang M, Ying P, Zhou L, Dong Y. Study of rock dynamic fracture toughness by using VB-SCSC specimens under medium–low speed impacts. *Eng Fract Mech.* 2017;181:52–64.
- [15] Zhou L, Zhu Z, Wang M, Ying P, Dong Y. Dynamic propagation behavior of cracks emanating from tunnel edges under impact loads. *Soil Dyn Earthq Eng.* 2018;105:119–26.
- [16] Ying P, Zhu Z, Zhou L, Wang M, Dong Y, Qiu H. The effect of loading rates on crack dynamic behavior under medium-low speed impacts. *Acta Mech Solida Sin.* 2019;32(1):93–104.
- [17] Wang Z, Ma L, Wu L, Yu H. Numerical simulation of crack growth in brittle matrix of particle reinforced composites using the xfem technique. *Acta Mech Solida Sin.* 2012;25(1):9–21.

- [18] Zhou X, Qian Q, Song H. The effects of three-dimensional penny-shaped cracks on zonal disintegration of the surrounding rock masses around a deep circular tunnel. *Acta Mech Solida Sin.* 2015;28(6):722–34.
- [19] Ma GW, An XM. Numerical simulation of blasting-induced rock fractures. *Int J Rock Mech Min Sci.* 2008;45(6):966–75.
- [20] Zhu WC, Bai Y, Li XB, Niu LL. Numerical simulation on rock failure under combined static and dynamic loading during SHPB tests. *Int J Impact Eng.* 2012;49:142–57.
- [21] Zhu WC, Li ZH, Zhu L, Tang CA. Numerical simulation on rockburst of underground opening triggered by dynamic disturbance. *Tunn Undergr Space Technol.* 2010;25(5):587–99.
- [22] Xu J, Li Z. Damage evolution and crack propagation in rocks with dual elliptic flaws in compression. *Acta Mech Solida Sin.* 2017;30(6):573–82.
- [23] Reddish DJ, Stace LR, Vanichkobchinda P, Whittles DN. Numerical simulation of the dynamic impact breakage testing of rock. *Int J Rock Mech Min Sci.* 2005;42(2):167–76.
- [24] Li M, Zhu Z, Liu R, Liu B, Zhou L, Dong Y. Study of the effect of empty holes on propagating cracks under blasting loads. *Int J Rock Mech Min Sci.* 2018;103:186–94.
- [25] Zhu Z, Wang C, Kang J, Li Y, Wang M. Study on the mechanism of zonal disintegration around an excavation. *Int J Rock Mech Min Sci.* 2014;67:88–95.
- [26] Wang M, Zhu Z, Dong Y, Zhou L. Study of mixed-mode I/II fractures using single cleavage semicircle compression specimens under impacting loads. *Eng Fract Mech.* 2017;177:33–44.
- [27] Dehghan Banadaki MM, Mohanty B. Numerical simulation of stress wave induced fractures in rock. *Int J Impact Eng.* 2012;40–41:16–25.
- [28] Wong LNY, Li HQ. Numerical study on coalescence of two pre-existing coplanar flaws in rock. *Int J Solids Struct.* 2013;50(22–23):3685–706.
- [29] Hongxiang J, Changlong D, Songyong L, Kuidong G. Numerical simulation of rock fragmentation under the impact load of water jet. *Shock Vib.* 2014;2014:1–11.
- [30] Li H, Wong LNY. Influence of flaw inclination angle and loading condition on crack initiation and propagation. *Int J Solids Struct.* 2012;49:2482–99.
- [31] Ma GW, Hao H, Zhou YX. Modeling of wave propagation induced by underground explosion. *Comput Geotech.* 1998;22(3–4):283–303.
- [32] Bagher Shemirani A, Naghdabadi R, Ashrafi MJ. Experimental and numerical study on choosing proper pulse shapers for testing concrete specimens by split Hopkinson pressure bar apparatus. *Constr Build Mater.* 2016;125:326–36.
- [33] Yao W, Xu Y, Yu C, Xia K. A dynamic punch-through shear method for determining dynamic mode II fracture toughness of rocks. *Eng Fract Mech.* 2017;176:161–77.
- [34] Yao W, Liu H, Xu Y, Xia K, Zhu J. Thermal degradation of dynamic compressive strength for two mortars. *Constr Build Mater.* 2017;136:139–52.
- [35] Yue Z, Song Y, Yang R, Yu Q. Comparison of caustics and the strain gage method for measuring mode I stress intensity factor of PMMA material. *Polym Test.* 2017;59:10–9.
- [36] Wang Y, Yang R, Zhao G. Influence of empty hole on crack running in PMMA plate under dynamic loading. *Polym Test.* 2017;58:70–85.
- [37] Zhang QB, Zhao J. A review of dynamic experimental techniques and mechanical behaviour of rock materials. *Rock Mech Rock Eng.* 2013;47(4):1411–78.
- [38] Zhu Z. Numerical prediction of crater blasting and bench blasting. *Int J Rock Mech Min Sci.* 2009;46(6):1088–96.
- [39] Zhu Z, Mohanty B, Xie H. Numerical investigation of blasting-induced crack initiation and propagation in rocks. *Int J Rock Mech Min Sci.* 2007;44(3):412–24.
- [40] Zhu Z, Xie H, Mohanty B. Numerical investigation of blasting-induced damage in cylindrical rocks. *Int J Rock Mech Min Sci.* 2008;45(2):111–21.
- [41] Zhu Z, Li Y, Xie J, Liu B. The effect of principal stress orientation on tunnel stability. *Tunn Undergr Space Technol.* 2015;49:279–86.
- [42] Zhou L, Zhu Z, Liu B. Influence of radial cracks on stability of surrounding rocks at different locations around tunnel. *Chin J Geotech Eng.* 2016;38(7):1230–7.
- [43] Zhou L, Zhu Z, Liu B. Influence of cracks on surrounding rock damage–failure mode of straight wall arch tunnel. *Rock Soil Mech.* 2017;38(12):3688–97.
- [44] Jiang F, Vecchio KS. Hopkinson bar loaded fracture experimental technique: a critical review of dynamic fracture toughness tests. *Appl Mech Rev.* 2009;62(6):1–9.